

# Formation of core-shell droplets for the encapsulation of liquid contents

Fariba Malekpour Galogahi

Griffith University

Yong Zhu

Griffith University

Hongjie An

Griffith University

Nam-Trung Nguyen (✉ [nam-trung.nguyen@griffith.edu.au](mailto:nam-trung.nguyen@griffith.edu.au))

Griffith University <https://orcid.org/0000-0003-3626-5361>

---

## Research Article

**Keywords:** Core-shell particle, Oil flow rate, Polymer flow rate, Shell thickness, Thermal stability

**Posted Date:** August 23rd, 2021

**DOI:** <https://doi.org/10.21203/rs.3.rs-835459/v1>

**License:** © ⓘ This work is licensed under a Creative Commons Attribution 4.0 International License.

[Read Full License](#)

---

# 1                    **Formation of core-shell droplets for the encapsulation of liquid contents**

2                    Fariba Malekpour Galogahi, Yong Zhu, Hongjie An, Nam-Trung Nguyen\*

3 Queensland Micro- and Nanotechnology Centre, Griffith University, 170 Kessels Road, 4111, Queensland, Aus-  
4 tralia

5 Corresponding Author: Nam-Trung Nguyen – Queensland Micro and Nanotechnology Centre, Griffith Univer-  
6 sity, Brisbane, Queensland 4111, Australia; orcid.org/0000-0003-3626-5361; Phone: +61-(07)-3735-3921; Email:  
7 [nam-trung.nguyen@griffith.edu.au](mailto:nam-trung.nguyen@griffith.edu.au); Fax: +61-(07)-3735-80211

## 8                    **Abstract**

9                    Accurate control of monodisperse core-shell droplets generated in a microfluidic device has a broad range of  
10 applications in research and industry. This paper reports the experimental investigation of flow-focusing micro-  
11 fluidic devices capable of producing size-tuneable and monodisperse core-shell droplets. The dimension of the  
12 core-shell droplets was controlled passively by the channel geometry and the flow rate of the liquid phases. The  
13 results indicate that microchannel geometry is more significant than flow rates. The highly controllable core-shell  
14 droplets could be subsequently employed as a template for generating core-shell microparticles with liquid core.  
15 Optical, electron microscopy and X-ray computed microtomography showed that the geometry of the core-shell  
16 droplets remains unchanged after solidification, drying and collection. The present study also looks at the thermal  
17 stability of core-shell particles depending on the particle size. The larger core-shell particles with a thicker shell  
18 provide a higher resistance to heating at elevated temperature. The high degree of control with a flow-focusing  
19 microfluidic device makes this a promising approach for the encapsulation, storage, and delivery of lipophilic  
20 contents.  
21

## 22                    **Keywords**

23 Core-shell particle, Oil flow rate, Polymer flow rate, Shell thickness, Thermal stability  
24

## 25                    **1. Introduction**

26 In recent years, droplets with a core-shell structure have attracted a considerable amount of interest due to their  
27 unique properties and potential applications. Monodisperse core-shell droplets can be used as a template to gen-  
28 erate microcapsules using various solidification techniques such as photo or thermal polymerization, solvent evap-  
29 oration, and ionic cross-linking (Xu and Nisisako 2020). Microcapsules of liquids are an important class of core-  
30 shell microcapsule with applications in food processing, cosmetics, controlled release as well as delivery of drugs,  
31 nutrients, and cells (Mytnyk et al. 2017; Wei et al. 2010). Conventional techniques for core-shell microcapsules  
32 production are layer-by-layer adsorption, polymerization, spray-drying, and electro-spraying (Galogahi et al.  
33 2020). However, these techniques suffer from lack of control over the size, structure, and process parameters,  
34 high materials consumption and low encapsulation efficiency, restricting the potential of the generated particles  
35 (Chong et al. 2015; Liu et al. 2011; Nabavi et al. 2017; Nisisako et al. 2005; Utada et al. 2005). Furthermore,  
36 surfactants are required to be used in most conventional emulsion techniques. The use of surfactants can cause  
37 delamination, corrosion (Lu et al. 2011), protein-surfactant adducts (Xiong et al. 2008), impurities (Zheng et al.  
38 2014), and quenching of fluorescence (Xie et al. 2009). The complete elimination of surfactants from the solutions  
39 is also cumbersome and time-consuming. Furthermore, the use of surfactants is not desirable for many clinical

40 applications (Hu et al. 2008). Surfactants may limit the potential development and practical applications of core-  
41 shell droplets. We therefore aim at surfactant-free formation of double emulsion in our encapsulation technique.

42

43 Microfluidic techniques could address the above challenges of conventional preparation techniques with  
44 well-controlled flow conditions (Nguyen et al. 1998). Droplet-based microfluidics provides a range of novel ap-  
45 plications, including enhanced heat and mass transfer (Bandara et al. 2015). Core-shell droplets generated using  
46 droplet-based microfluidics are highly monodispersed and uniform. The generated droplets can be further con-  
47 trolled by various means (Yap et al. 2009). Microfluidic core-shell droplets are generated with a relatively precise  
48 and tunable control over the size, the shell thickness, and the shape of droplets. One of the most efficient geome-  
49 tries for the generation of size-tunable droplets is a flow-focusing geometry (Lashkaripour et al. 2019; Lee et al.  
50 2009). However, the underlying physics and mechanisms of droplets generation in flow-focusing geometry has  
51 not yet been fully understood, hindering its performance in practical applications (Liu and Zhang 2011). To date,  
52 a large number of investigations focused on the role of physical and geometrical parameters of flow-focusing  
53 droplet generation (Costa et al. 2017; Lignel et al. 2017; Rahimi et al. 2019; Wang et al. 2019). For instance, Lee  
54 et al. (Lee et al. 2009) investigated experimentally the generation of tuneable droplets in flow focusing geometries.  
55 The authors defined relevant dimensionless parameters for flow-focusing microfluidic devices. By varying these  
56 parameters, they showed that single droplet formation depends on the viscosities, interfacial tension, flow rate of  
57 the fluids, and the device's geometry. Many studies have previously discussed single droplets generation in flow-  
58 focusing geometry and the effects of geometrical and physical parameters on droplet formation (Carneiro et al.  
59 2016; Lashkaripour, Rodriguez et al. 2019; Lignel, Salsac et al. 2017; Ward et al. 2005). Liao et al. (Liao et al.  
60 2018) and Wang et al. (Wang et al. 2019) investigated the effect of fluid flow rates on the size of core-shell  
61 particles with aqueous core in a flow focusing geometry. Furthermore, a variety of materials has been used to  
62 manufacture the devices with diverse geometry. Droplet formation mechanism and behaviour could vary with the  
63 materials used to fabricate the device, device geometry, fluid properties and operation conditions. Consequently,  
64 the results obtained are inconclusive. The challenge is to accurately determine the operating condition of the  
65 experiment based on optimised parameters to ensure the desired droplet size.

66 The present paper reports a PDMS-based microfluidic device for the controllable production of surfac-  
67 tant-free core-shell particles, using core-shell droplet as a template. We utilised flow-focusing microfluidic de-  
68 vices with a hydrophilic surface to generate the core-shell droplets, which enables the production of core-shell  
69 microparticles consisting of a HFE7500 fluorinated oil core and a polymer shell of trimethylolpropane trimethac-  
70 rylate (TMPTMA). We demonstrated that the size of the core and the shell thickness can be tuned accurately and  
71 flexibly by adjusting the dimension of the channels and the fluid flows. One key parameter for the successful  
72 fabrication of core-shell particles with different sizes was the width of the main channel. We further investigated  
73 the formation mechanisms of HFE 7500 oil core droplets and proposed a model to predict the core size. The model  
74 predicts the core slug length as a function of geometrical and physical variables. Optical, scanning electron mi-  
75 croscopy and X-ray computed micro tomography were utilised to investigate the morphology of the resulting  
76 core-shell particles. The results indicate that the core-shell structures remain stable during the collection and dry-  
77 ing process. To further understand the robustness of the particles at elevated temperature, we also extend our  
78 studies to the behaviour of the core-shell particles under heating.

79

## 80 2. Materials and Methods

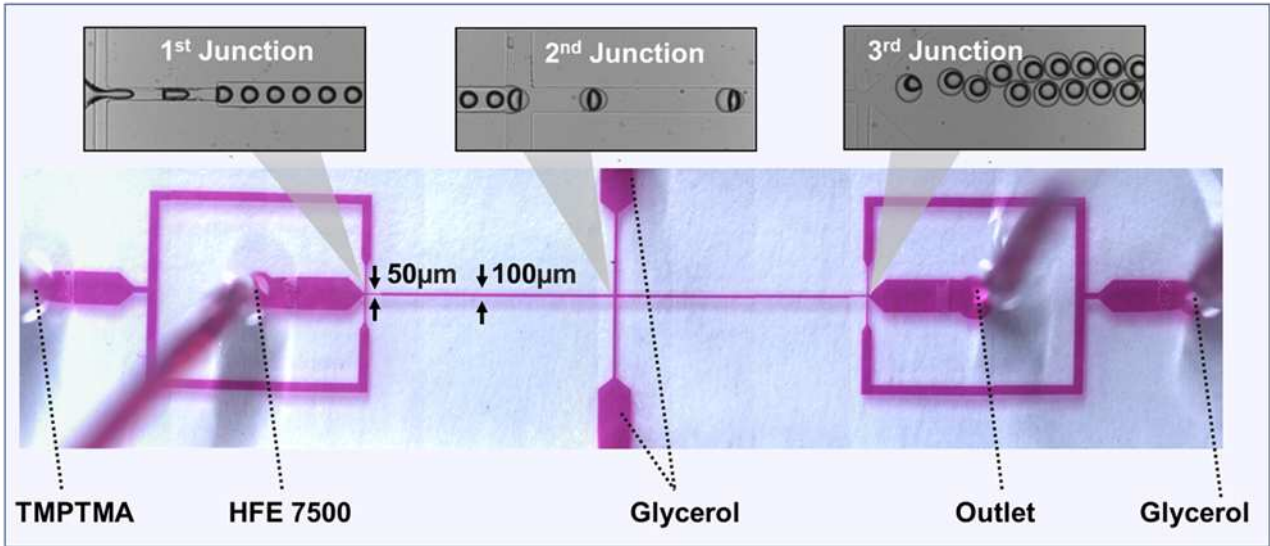
### 81 2.1. Materials

82 Fluorinated oil (HFE, Novec 7500 3M) with a surface tension of  $\sigma_{oil} = 15.52$  mN/m, a viscosity of  $\mu_{oil} = 1.31$  cP,  
83 a density of  $\rho_{oil} = 1.63$  g/ml and a boiling point of  $128^\circ$  C was used as the liquid phase for the core (oil phase)  
84 (Rausch et al. 2015). The shell liquid (polymer phase) comprised of 0.06 g ethyl- 4(dimethylamino)benzoate  
85 (Merck), 0.05 g camphorquinone (Merck), and 10 g of trimethylolpropane trimethacrylate (TMPTMA, Merck).  
86 The surface tension, viscosity, and density of the polymer solution are  $\sigma_{polymer} = 32.5$  mN/m,  $\mu_{polymer} = 42$  cP, and  
87  $\rho_{polymer} = 1.07$  g/ml, respectively (Takei et al. 2019). An aqueous solution of 50% glycerol (Chemsupply,  $\sigma_{polymer} =$   
88  $67$  mN/m,  $\mu_{polymer} = 6$  cP, and  $\rho_{polymer} = 1.12$  g/ml) in distilled water was utilised as the outer continuous phase  
89 (Gregory 2018).

### 90 2.2. Microfabrication

91 We first used the PDMS-based microfluidic device introduced in our previous preliminary study to generate core-  
92 shell droplets (Teo et al. 2020). The device was fabricated using soft lithography. Two master moulds were pre-  
93 pared with respective channel widths of  $100\ \mu\text{m}$  and  $200\ \mu\text{m}$  and respective channel constriction with widths of  
94  $50\ \mu\text{m}$  and  $100\ \mu\text{m}$  to investigate the effect of channel geometry on droplet size. The second device with the  
95 channel constriction width of  $100\ \mu\text{m}$  has an inlet neck of  $70\ \mu\text{m}$ . The height  $h$  of all channels are  $100\ \mu\text{m}$  in both  
96 devices. A mixture of PDMS and curing agent (volume ratio of 10: 1) was poured onto the master mould. After  
97 curing at  $75^\circ\text{C}$  for 1 hour, the PDMS substrate was removed from the master mould. The inlets and outlet were  
98 created using a biopsy puncher. Subsequently, the PDMS substrate was bonded onto a glass substrate. Permanent  
99 bond was obtained after an air plasma treatment of both PDMS and the glass substrate in a low-pressure plasma  
100 cleaner. Finally, passing distilled water along the channels of the PDMS device keeps them sufficiently hydro-  
101 philic for the later experiments.

102 Figure 1 shows the fabricated device with the three cross junctions. The microchannels were visualised  
103 with food dye. The core-shell droplets are generated in three steps. First, the core droplets are formed at the first  
104 cross junction and dispersed into a flow of the shell prepolymer liquid. Hydrophobic TMPTMA monomer was  
105 chosen as the shell material, due to high thermal stability (Matsumoto et al. 2010) and high strength of its cross-  
106 linked network after polymerization (Takei et al. 2019). TMPTMA is commonly used in dentistry and does not  
107 show any evidence of toxic effects. The TMPTMA solution was prepared at a concentration of 98 mol% according  
108 to a previous report, and thus maintain the spherical shape and stable dimension of the core-shell particle af-  
109 ter polymerization (Gorgannezhad et al. 2020; Sreejith et al. 2020). Next, the core droplets delivered into the  
110 second junction are encapsulated by the shell liquid to generate a core-shell droplet in a continuous phase of 50%  
111 glycerol solution. Glycerol increases the viscosity of the continuous phase, which results in a higher shear at the  
112 second junction and accelerates the pinch-off process of the shell layer. Finally, the core-shell droplets move  
113 through the channel to the third junction, where the droplets are separated further apart by 50% glycerol solution  
114 serving as the spacer fluid to prevent coalescence.



116 **Figure 1** The PDMS microfluidic device with three cross junctions for the generation of core-shell droplets in the  
 117 first device with the channel width of 100µm and channel constriction width of 50 µm. The core-shell droplets  
 118 are produced in two steps. The core droplets are formed at the first cross junction, and are further encapsulated by  
 119 the shell liquid to generate a core-shell droplet at the second cross junction. Finally, the core-shell droplets are  
 120 delivered into the third junction and are further separated apart by the spacer fluid to prevent accidental coales-  
 121 cence.

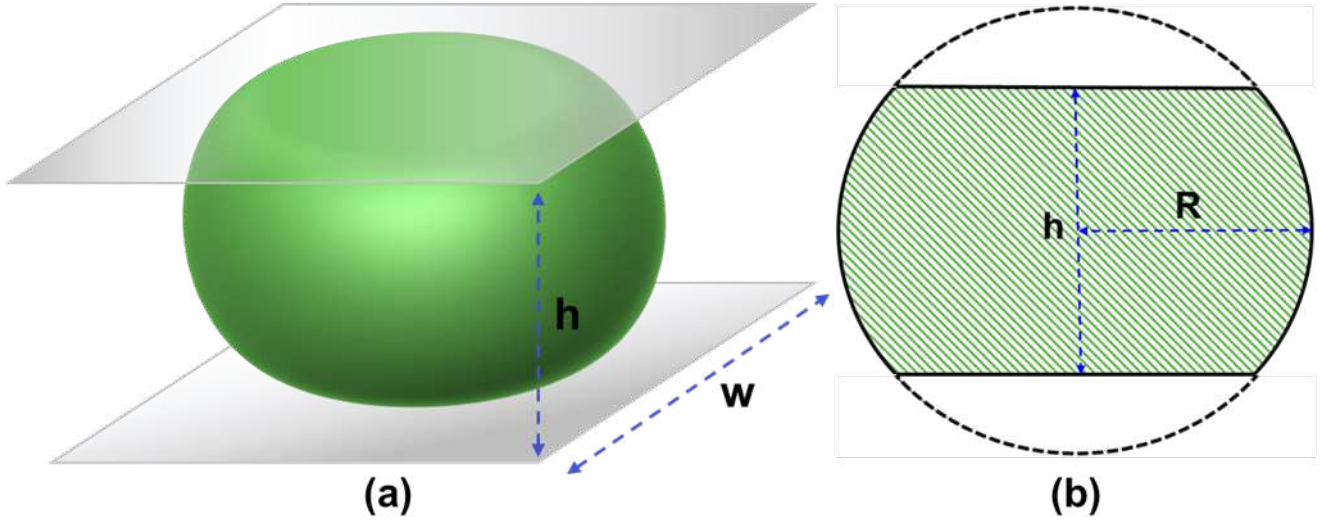
### 122 2.3. Experimental setup and procedure

123 The PDMS device was placed on an inverted microscope (Nikon, Eclipse Ti) for real-time recording of the core-  
 124 shell droplet generation. The video was captured with a 10× objective lens in brightfield mode. We employed a  
 125 syringe pump interfaced to a computer for controlling the flow rates of all fluids. The flow rates of the core fluid  
 126 and the shell fluid were varied and investigated to identify the effects of flow conditions on the core-shell emul-  
 127 sion. First, the core flow was varied from 60 to 140 µL/hr, while the flow rates of the shell fluid and glycerol  
 128 solution at the second and the third cross junctions were maintained at 150, 800 and 1,600 µL/hr, respectively.  
 129 Next, the flow rate of the shell fluid was varied from 130 to 190 µL/hr, while the flow rates of core fluid and  
 130 glycerol solution at the second and third junctions were fixed at 100, 800 and 1,600 µL/hr, respectively.

### 131 2.4. Characterization of core-shell droplets and particles

132 All recorded videos were evaluated with the ImageJ software to determine the area of the core droplets  $A_{\text{Core}}$  and  
 133 core-shell droplets  $A_{\text{Core-shell}}$  and the separation distance in the channels. Subsequently, the equivalent radius of  
 134 the droplets  $R_{\text{eq}}$  was calculated as  $R_{\text{eq}} = \sqrt{A/\pi}$  where  $A$  is the droplet area. All the experiments and measurements  
 135 were carried out three times. In each experiment, the area of 30 droplets was evaluated.

136 Figure 2 shows the model of the core-shell droplet in a microchannel with the channel height is less than the  
 137 droplet diameter ( $h < 2R_{\text{eq}}$ ). In this case, the droplet is considered as a discoid.



139 **Figure 2** (a) Schematic illustration of core-shell droplet squeezed into a discoid shape between the channel  
 140 walls and (b) side view of the droplet

141 Thus, the geometric parameters of the droplets can be directly derived from the height of channel  $h$  and the radius  
 142 of the discoid  $R$ . The volume  $V_{\text{discoid}}$  of the core-shell droplets in both devices and the core droplets in second  
 143 device with discoid shape can then be derived as (Nie et al. 2008; Teo et al. 2020):

$$144 \quad V_{\text{discoid}} = \frac{\pi}{12} [16R^3 - (2R - h)^2 (4R + h)] \quad (1)$$

145 If the diameter of droplet is less than the channel height, such as in the case of the core droplet in the later exper-  
 146 iments with a channel width of 100  $\mu\text{m}$ , the droplets remain the spherical. Assuming the final hardened particle  
 147 is a sphere, the radius of the core droplet  $R_{\text{core}}$ , the discoid core droplet  $R'_{\text{core}}$ , and the radius of discoid core-  
 148 shell droplet  $R_{\text{core-shell}}$  and the thickness of the shell  $T$  are determined as:

$$149 \quad R_{\text{core}} = \sqrt{\frac{A_{\text{core}}}{\pi}} \quad (2)$$

$$150 \quad R'_{\text{core}} = \sqrt[3]{\frac{3V_{\text{discoid}}}{4\pi}} \quad (3)$$

$$151 \quad R_{\text{core-shell}} = \sqrt[3]{\frac{3V_{\text{discoid}}}{4\pi}} \quad (4)$$

$$152 \quad T = R_{\text{core-shell}} - R_{\text{core}} \quad (5)$$

$$153 \quad T = R_{\text{core-shell}} - R'_{\text{core}} \quad (6)$$

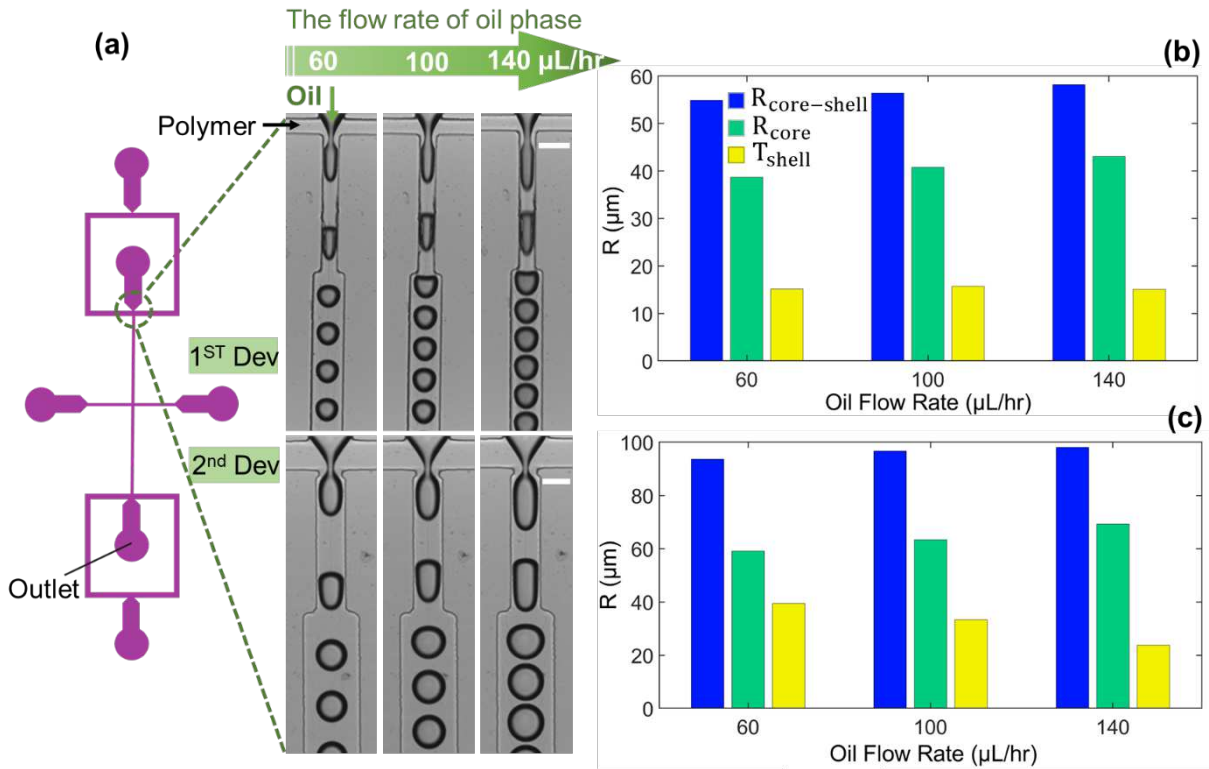
154 To ensure the accuracy of the above geometry estimation, data obtained with droplets along the channels  
 155 using these equations was compared with the solidified particles diameter measured after collection and solidifi-  
 156 cation. The results show that the difference in the core and core-shell droplet size and shell thickness gained  
 157 through these two methods is less than 3%. Optical microscopy, scanning electron microscopy (SEM) (JEOL,  
 158 JSM-6510LV) and X-ray computed microtomography were applied to investigate the morphology and geomet-  
 159 rical properties of the core-shell particles. The core-shell droplets were collected at the outlet. The collected solu-  
 160 tion with core-shell droplets was exposed to UV irradiation for 5 minutes by an UV source at a wavelength of

161  $\lambda=365$  nm. After polymerisation of the shell layer and the formation of solid beads, the collected samples were  
162 air-dried at room temperature for 3 days. Optical microscopy images of the collected samples were taken with a  
163 microscope (Eclipse Ti2, Nikon) and a high-speed camera at a maximum frame rate of 320 fps at a full resolution  
164 of  $2136 \times 2136$  pixels. SEM and optical images were analysed by the ImageJ software to measure the diameter of  
165 the core-shell droplet and core and shell thickness. The three-dimensional (3D) microstructure of core-shell parti-  
166 cles was assessed with high-resolution X-ray microtomography. 3D imaging was obtained using an X-ray com-  
167 puted microtomography system (VersaXRM-500 High-Resolution 3D X-ray Tomography Microscope System,  
168 ZEISS® Xradia, Pleasanton, CA, USA). The measurement was conducted by applying a constant voltage of 40 kV  
169 and a power of 3 W, with air filter and 20 s exposure time. The source detector distance was adjusted to  
170 20 mm, with a total magnification of  $20\times$  resulting in a pixel size of  $0.2891 \mu\text{m}$  and a field of view (FOV) of  
171 approximately  $576 \mu\text{m} \times 576 \mu\text{m}$ .

172         Microparticles with two sizes were prepared with the two microfluidic devices mentioned above. The  
173 samples were heated steadily from  $27^\circ\text{C}$  using a heater until a change in the particle surface was detected. The  
174 microparticles were kept at the constant temperature for 10 min under ambient atmosphere. If no change was  
175 observed, the temperature was increased by  $5^\circ\text{C}$ , followed by a 10 min at the constant temperature. During the  
176 heating process, particles were monitored and top view of them was recorded using a camera (Ximea xiQ-USB3  
177 MQ013CG-ON) and a high-resolution magnification lens (Edmund Optics).

### 178     **3. Results and Discussion**

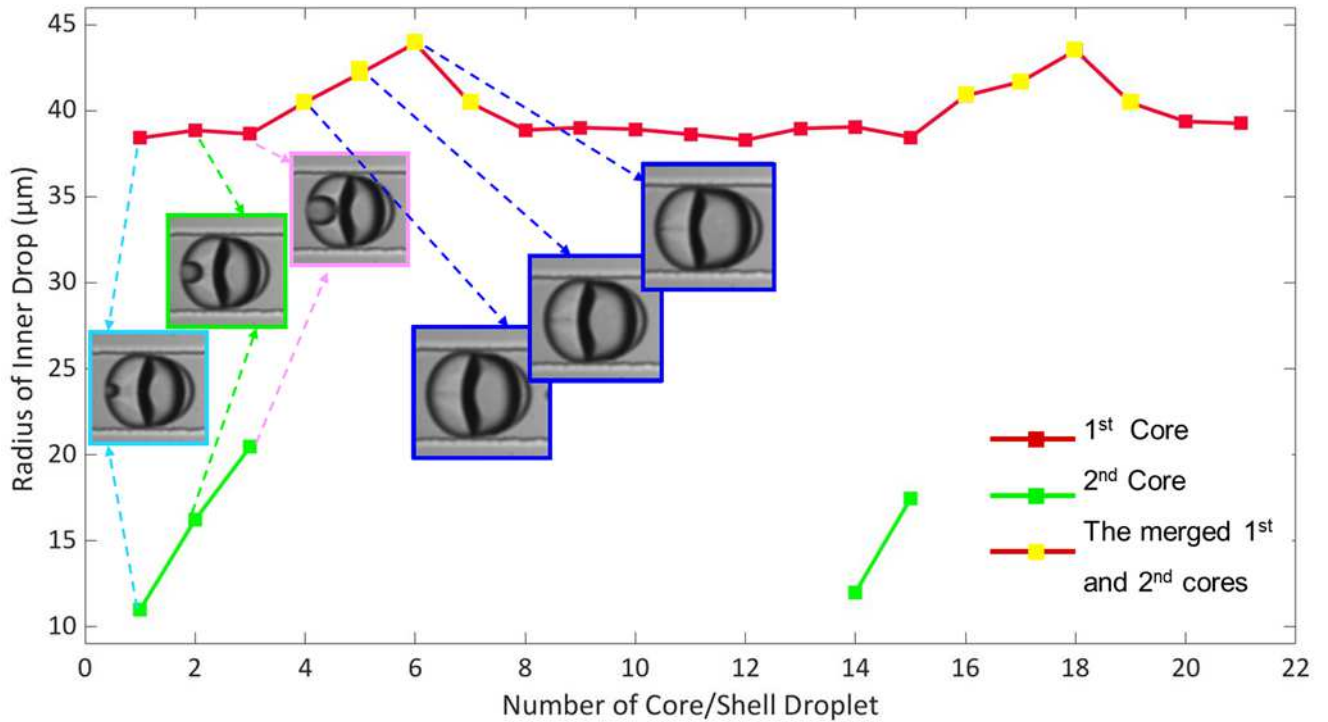
179     Figure 3 shows the impact of the change in oil flow rate on the core and core-shell droplet size and the shell  
180 thickness in the two microfluidic devices. The channel width of the first and second device was  $100 \mu\text{m}$  and  
181  $200 \mu\text{m}$ , respectively. Figure 3(a) shows that increasing the oil flow rate from  $60 \mu\text{L/hr}$  to  $140 \mu\text{L/hr}$  slightly  
182 increase the radius of the core in both devices. The formation of droplets in the flow-focusing geometry relies on  
183 the interplay between the shear and interfacial forces. The drop breaks up when the shear force overcomes the  
184 interfacial tension (Costa et al. 2017). A higher flow rate of the core phase allows more core liquid to accumulate  
185 before the breakup, resulting in a larger droplet. A slight increase of the core-shell droplet radius was observed in  
186 both devices, Fig. 3(b, c). With increasing flow rate, the thickness of the shell remains almost constant in the first  
187 device, while the thickness in the second device decreases gradually, Figs. 3(b, c). Comparing Fig. 3(b) and Fig.  
188 3(c) indicates that the core and core-shell droplets radius were sensitive to the width of channels and larger droplets  
189 were produced in a broader channel. The radius of the generated core droplets and core-shell droplets increased  
190 by about 50%- 60% and 60%-80% respectively by doubling the channel width.



192 **Figure 3** Core-shell droplet geometry as function of core flow rate: (a) Images from recorded videos showing  
 193 formation of core droplets with changeable size at different oil flow rate in first device (1<sup>st</sup> Dev) and second device  
 194 (2<sup>nd</sup> Dev); Influence of the oil flow rate on the radius of core-shell droplets  $R_{core-shell}$  and the core  $R_{core}$  and the  
 195 shell thickness  $T_{shell}$  in (b) in the first microfluidic device and (c) second microfluidic device. Scale bars depict  
 196 100 μm

197 Figure 3(a) shows that increasing the oil flow rate decreases the separation distance between the core  
 198 droplets. Altering the flow rates also affects subsequently the number of core droplets encapsulated within the  
 199 outer shell. At 60 μL/hr, the distance between the core droplets is larger than the major axis length of the core-  
 200 shell droplets; hence we observed some droplets without core in both devices. The optimal oil flow rates and shell  
 201 flow rates for achieving uniform core-shell droplets with a single core droplet was 100 μL/hr and 150 μL/hr and  
 202 70 μL/hr and 150 μL/hr in first and second device, respectively.

203 If the distance between core droplets is greater than the major axis length of the core-shell droplet, uni-  
 204 form droplets were generated. In the first device with the 100-μm channel width, the formation of compact core  
 205 droplets at 140 μL/hr in the first junction led to the generation of unstable core-shell droplets containing two cores.  
 206 Figure 4 depicts the radius of the encapsulated first and second core droplets with respect to the number of drop-  
 207 lets. We observed that the radius of first core droplet remained unchanged while the radius of the second core  
 208 gradually grew. However, further growth of the second core droplet beyond a threshold resulted in the coalescence  
 209 of the two core droplets immediately after the formation in the second junction.



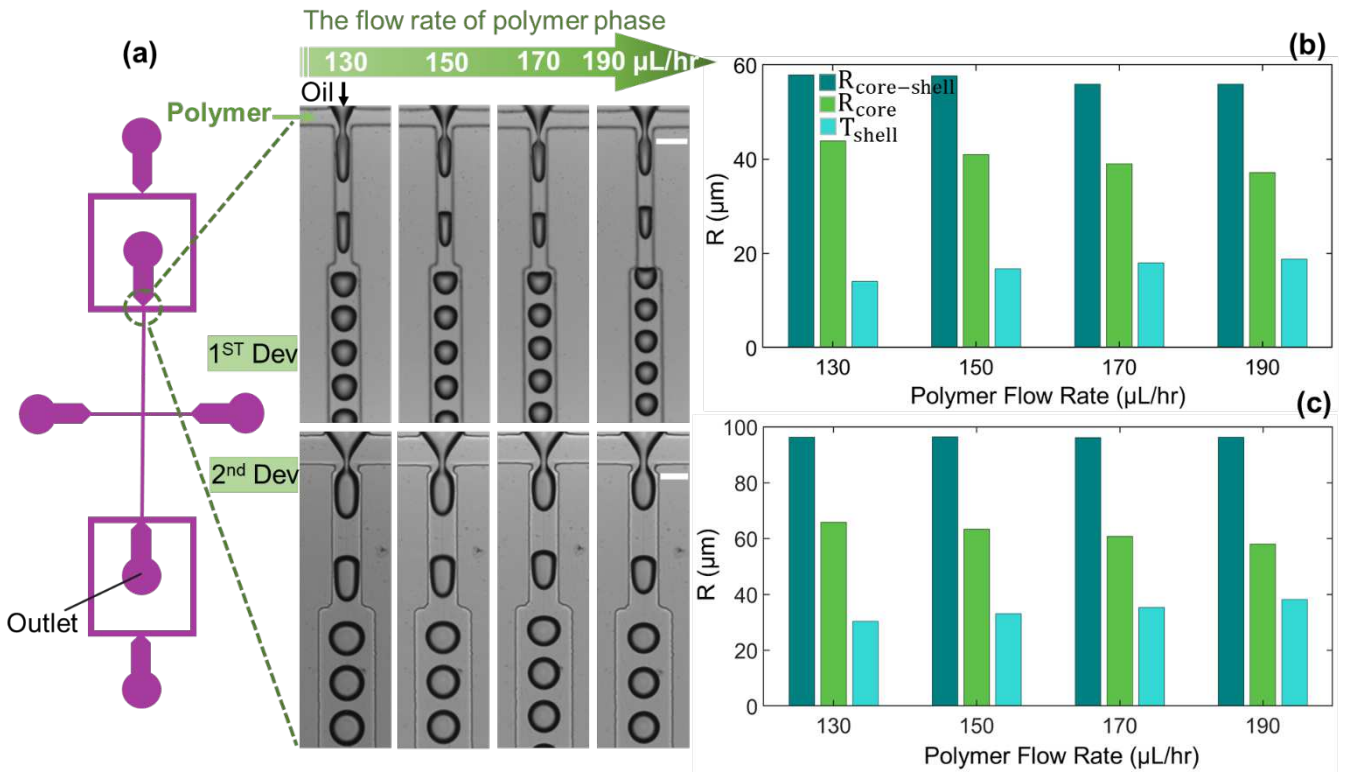
210  
211

**Figure 4** Variation of the radius of first and second core with the sequence number of core-shell droplets

212

Figures 5 show the influence of varying the shell flow rate on the geometry of the core-shell droplets. A high degree of control on the dimensions of the core droplet and the shell was achieved. Flow rates of the core and glycerol at the second junction and at the third junction were fixed at 100  $\mu\text{L/hr}$ , 800  $\mu\text{L/hr}$  and 1,600  $\mu\text{L/hr}$ , respectively. The droplet images in Fig. 5(a) indicate that the separation distance between the cores formed at the first junction remain constant in both devices. Increasing the flow rate of the shell from 130  $\mu\text{L/hr}$  to 190  $\mu\text{L/hr}$  resulted in a slight reduction in radius of both core and core-shell droplet in both devices. Increasing the polymer flow rate results in a shorter time for the growth of the core and the formation of shell layer.

218

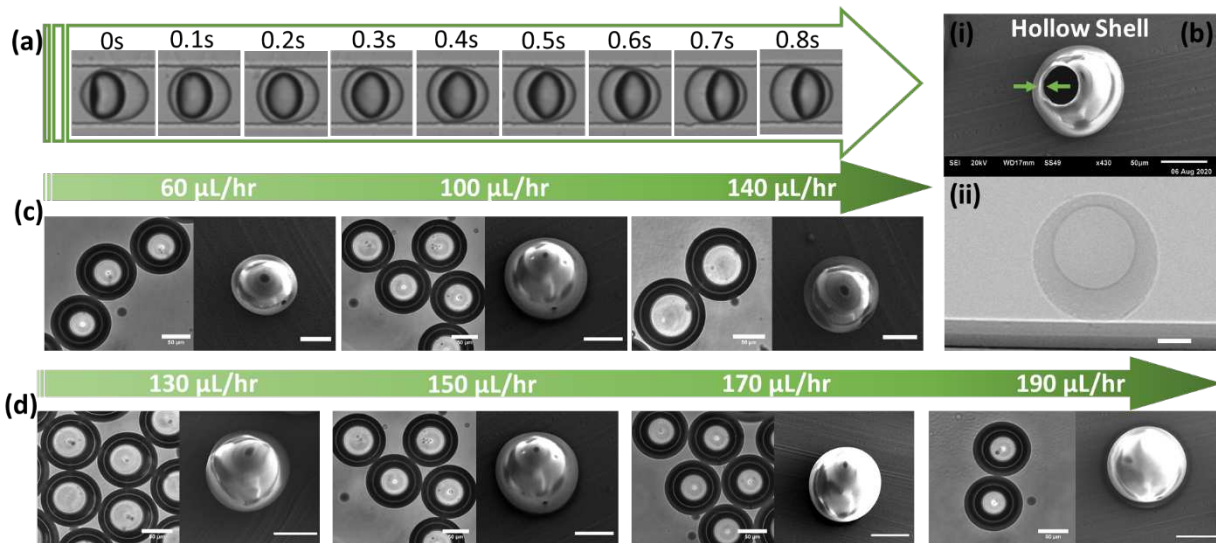


220 **Figure 5** Core-shell droplet geometry as function of shell flow rate: (a) Images from recorded videos presenting  
 221 core droplets with varying radius at different polymer flow rate in the first device (1<sup>st</sup> Dev) and the second device  
 222 (2<sup>nd</sup> Dev); The radius of core-shell droplets  $R_{core-shell}$  and the core  $R_{core}$  and the shell thickness  $T_{shell}$  as a  
 223 function of the polymer flow rate in (b) in the first microfluidic device and (c) second microfluidic device. Scale  
 224 bars depict 100 μm

225 Furthermore, a higher flow rate of the polymer leads to a higher shear force between the two phases,  
 226 contributing to a faster breakup and a smaller core droplet, Figs. 5 (a, b). Figures 5 (b, c) indicate an increase in  
 227 the shell thickness with increasing polymer flow rate in both devices. Unlike the slight effect of polymer flow rate  
 228 on the core and core-shell droplet size and shell thickness, experimental results clearly confirm that they can be  
 229 remarkably affected by the channel geometry, Figs. 5 (b, c). The radius of the core and core-shell droplet of the  
 230 second device were almost twice that of the first device.

231 In the above investigations, all measurements were conducted after the core-shell droplets were stabilised  
 232 in the microchannel. The core-shell droplets are deformed while passing through the microchannel. Hence, we  
 233 subsequently investigated the deformation of the core in the core-shell droplets along the channel between the  
 234 second junction and the outlet. We employed the optimized oil and polymer flow rates achieved in our preliminary  
 235 work (Teo et al. 2020). The optimum flow rates for oil, polymer and glycerol at the second and third junction  
 236 were 100 μL/hr, 150 μL/hr, 800 μL/hr, and 1,600 μL/hr, respectively. Figure 6(a) shows the different position of  
 237 core-shell droplet during the passage with respect to time. While the core-shell droplets move from the second  
 238 junction to the outlet, image frames were extracted for the same droplet. The first image at 0 sec is the frame of  
 239 the core-shell droplet just after the pinch-off, Fig. 6(a). The last image is the frame of core-shell droplets after  
 240 stabilisation along the microchannel. The deformation of the core droplet is visible. The core-shell droplet pro-  
 241 trudes into the glycerol phase and is sheared by the glycerol phase. The continuous phase pushes the core-shell  
 242 droplet forward along the microchannel. While the droplet passes through the channel, the low interfacial tension

243 between the polymer and the core liquid allows the shape of the droplet to deform considerably. The deformation  
 244 is also caused by the internal circulation of the polymer phase.  
 245



246 **Figure 6** (a) A time series of images displaying the deformation of inner drop encapsulated into the shell be-  
 247 tween the second junction and outlet. (b) (i) Scanning electron microscopy image of an open hollow shell and  
 248 (ii) X-ray image of an intact core-shell particle; (c) The flow rate of the inner phase in the first device with the  
 249 width of 100  $\mu\text{m}$  (oil); (d) The flow rate of shell phase (polymer) in the device with the width of 100  $\mu\text{m}$ . The  
 250 scale bar corresponds to 50  $\mu\text{m}$

251 The morphologies of core-shell particles were observed using SEM and X-ray computed microtomogra-  
 252 phy (Fig. 6). The SEM images confirmed that the core-shell particles have a spherical shape and a smooth surface.  
 253 As the SEM micrographs can only provide an image of the shell, X-ray computed microtomography was employed  
 254 to analyse the entire core-shell structure after solidification and drying. The X-ray image confirmed the well-  
 255 defined core-shell structure of particles, Fig. 6 (b,ii). The impacts of the flow rates of core and shell phases were  
 256 further studied using scanning electron and optical microscopy. Figures 6 (c, d) show the scanning electron mi-  
 257 croscopy (SEM) images and optical images of samples at different core and shell flow rates. The core-shell drop-  
 258 lets with different dimensions with corresponding flow rates could be observed with optical microscopy images  
 259 (Figures 6 (c, d)), confirming the fabrication of size-tunable core-shell droplets. Both SEM and optical images  
 260 agreed with the data gained through measuring the size of the core-shell droplets along the channel.

261 We subsequently investigated the core droplet formation at the first junction in the flow-focusing geom-  
 262 etry, Figure 7. The microchannel after the first junction has a width of  $w$  and a constriction region of width  $D$ .  
 263 The values of  $w$  and  $D$  are 100  $\mu\text{m}/50 \mu\text{m}$  and 200  $\mu\text{m}/100 \mu\text{m}$  for the first and second device, respectively. The  
 264 generalised behaviour of fluid flows in a flow-focusing microfluidic device can be described by a number of  
 265 dimensionless numbers, which capture the geometrical and physical parameters such as flow rates, the interfacial  
 266 tension, viscosities and densities of the fluids, and the dimensions in the device. In microchannels, the value of  
 267 Reynolds and Weber numbers are typically relatively small due to the channel size and the low flow rate of the  
 268 fluids; the inertial effect of the flow field can therefore be ignored (Costa, Gomes et al. 2017). On the other hand,  
 269 the capillary number that represents the relative effect of viscous stress versus interfacial tension plays an im-  
 270 portant role in the process of droplet formation in microfluidic devices (Liu and Zhang 2009; Liu and Zhang  
 271 2011). The capillary number is defined as:

272 
$$Ca = \frac{\eta_{\text{Polymer}} u_{\text{Polymer}}}{\sigma_{\text{Oil,Polymer}}} = \frac{\eta_{\text{Polymer}} Q_{\text{Polymer}}}{hw\sigma_{\text{Oil,Polymer}}}, \quad (7)$$

273 where  $\eta_{\text{Polymer}}$ ,  $u_{\text{Polymer}}$ , and  $Q_{\text{Polymer}}$  are the viscosity, the inlet velocity, and the flow rate of the continuous  
 274 phase (polymer), respectively.  $\sigma_{\text{Oil,Polymer}}$  refers to the interfacial tension between the dispersed phase (oil) and  
 275 the continuous phase (polymer). Good and Girifalco proposed a model for the interfacial tension for liquid-liquid  
 276 systems (Good and Girifalco 1960):

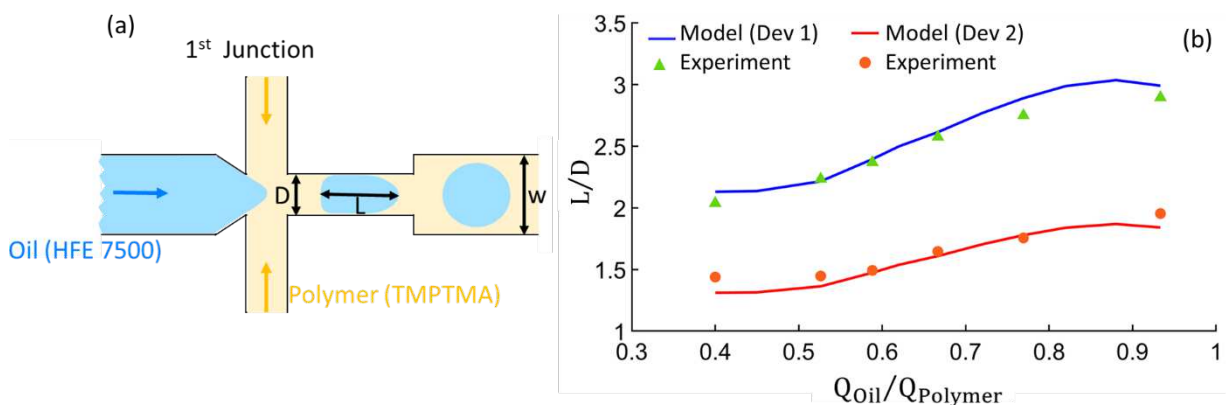
277 
$$\sigma_{\text{Oil,Polymer}} = \sigma_{\text{Oil}} + \sigma_{\text{Polymer}} - 2\Phi(\sigma_{\text{Oil}}\sigma_{\text{Polymer}})^{1/2}, \quad (8)$$

278 where  $\sigma_{\text{Oil}}$  and  $\sigma_{\text{Polymer}}$  are the surface tensions of the oil phase and the polymer phase, respectively;  $\Phi$  is the  
 279 interaction coefficient given as  $\Phi = 4(V_{\text{Oil}}V_{\text{Polymer}})^{1/2}/(V_{\text{Oil}}^{1/2} + V_{\text{Polymer}}^{1/2})^2$ , where  $V_{\text{Oil}}$  and  $V_{\text{Polymer}}$  are the mo-  
 280 lar volume of the oil phase and polymer phase, respectively. In our case, because of the small difference between  
 281  $V_{\text{Oil}} = 256.5$  ml/mol and  $V_{\text{Polymer}} = 293.86$  ml/mol the value of  $\Phi = 0.99$  was considered as unity. The in-  
 282 terfacial tension estimated from equation (8) is  $\sigma_{\text{Oil,Polymer}} = 3.10$  mN/m. The flow rate ratio of dispersed phase  
 283 flow rate to continuous phase  $Q_{\text{Oil}}/Q_{\text{Polymer}}$  is another important dimensionless parameter for droplet formation.

284 Two important factors affecting the size of core droplets at the first junction in a flow-focusing system  
 285 are (i) wetting properties and properties of fluids interface, which can be influenced by the ratio of dispersed phase  
 286 flow rate to continuous phase flow rate and the geometrical parameters; and (ii) the relative effect of viscous forces  
 287 of the continuous phase versus interfacial tension represented by the capillary number (Tan et al. 2008). To predict  
 288 the core slug or core droplet size at the first junction, we define the ratio of the slug length  $L$  to the width  $D$  of the  
 289 constricted section as a function of geometrical parameters,  $Q_{\text{Oil}}/Q_{\text{Polymer}}$ , and the capillary number,

290 
$$\frac{L}{D} = 1.3 \frac{h}{w} \left( \frac{Q_{\text{Oil}}}{Q_{\text{Polymer}}} \right)^{0.4} Ca^{-0.3} \quad (9)$$

291 We determined the constants of the equation experimentally through curve fitting across all experiments  
 292 conducted by using both flow-focusing devices. For both set of experiments carried out for the two two different  
 293 geometries, we calculated the capillary number for each experiment using equation (7). Figure 7(b) shows the two  
 294 sets of data obtained from two devices with different channel widths. Figure 7(b) indicates that this model fits  
 295 well with experimental data across the range of investigated flow rates and channel geometries. The ratio of  $L/D$   
 296 increases with increasing ratio  $Q_{\text{Oil}}/Q_{\text{Polymer}}$ .

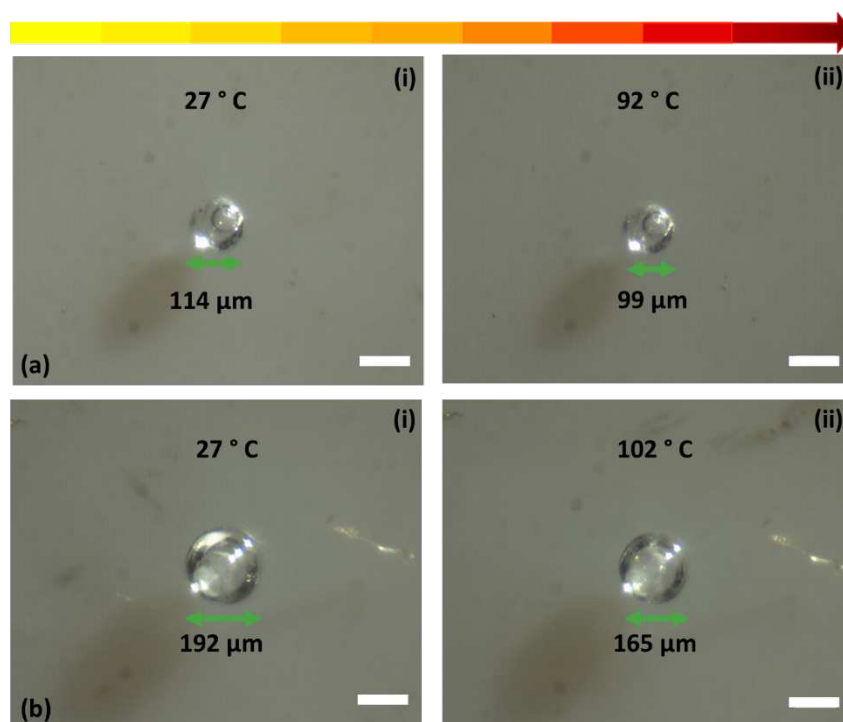


297 **Figure 7** (a) Schematic illustration of the core droplet formation at the first junction of a flow-focusing microflu-  
 298 idic device, (b) the ratio of slug length to the channel contraction width as a function of ratio of dispersed phase  
 299 flow rate to continuous phase flow rate.

300

301 We further studied the thermal stability of core-shell particles from the two devices. As mentioned above,  
 302 the device width has significant impact on the particle geometry. The microfluidic devices mentioned above pro-  
 303 duced two particle samples with a considerable size difference. Particles were generated at the optimum flow  
 304 rates. The overall radius of the particles and shell thickness were  $57\ \mu\text{m}$  and  $16\ \mu\text{m}$  in the first device and  $96\ \mu\text{m}$   
 305 and  $33\ \mu\text{m}$  in the second device, respectively. Figure 8 shows the temperature dependence of the core-shell parti-  
 306 cle size and the shell thickness. In the case of particles formed in the first device, which are smaller and have a  
 307 thinner shell, the morphology of particles remains unaffected up to  $92^\circ\text{C}$ . Larger particles with thicker shell  
 308 formed in the second device remain stable until  $102^\circ\text{C}$ . Both temperature values are below the boiling temperature  
 309 of the oil at  $128^\circ\text{C}$ . Thus, the core-shell particles are substantially stable up to these elevated temperatures. At the  
 310 critical rupture temperature, the particle shell ruptures and shrinks. The gradual shrinking of the solid shell could  
 311 be attributed to the release of oil core and deflation of the polymeric shell due to the reduced pressure. Comparing  
 312 the images of the first and second device before and after heating, we observed that the polymer shell of the larger  
 313 particle is more robust against heating. This might be due to the thicker wall resisting the increasing pressure of  
 314 the heated liquid core.

315



316 **Figure 8** Core-shell particles produced in the first device: (a) before and (b) after heating up to  $92^\circ\text{C}$ ; Core-shell  
 317 particles produced in the second device: (c) before and (d) after heating up to  $102^\circ\text{C}$ . The scale bar is  $100\ \mu\text{m}$ .

#### 318 4. Conclusion

319 This paper presents the tuneable generation and the characterisation of core-shell particles in a flow-focusing  
 320 PDMS microfluidic device. Varying the experimental parameters allowed for identification of the best condition  
 321 to produce desirable core-shell particles, enabling the control of particle geometries and stability. A procedure  
 322 was adopted for tuning precisely core-shell particle geometry based on fluid flow rate and device geometry. In-  
 323 dependently varying oil phase and polymer phase flow, particles with different core number, core size and shell  
 324 thickness were obtained. For the same flow rates, the experimental results indicate that the channel width is the  
 325 most important parameter affecting core-shell particle geometry. The wider channels resulted in larger core and

326 core-shell droplets as well as a thicker shell. The investigation on the influences of a group of geometrical and  
327 physical factors on the size of the core droplets at the first junction showed that there is a reasonable relationship  
328 between the ratio of the core slug length to the channel contraction width and capillary number, the ratio of height  
329 to width of channel, and the ratio of dispersed phase flow rate to continuous phase flow rate. Equation 9 could  
330 describe this relationship well. The analytical results showed a good agreement with experimental data. The core-  
331 shell droplets can be polymerised and solidified to generate spherical particles with liquid core and polymer shell.  
332 In the end, the core-shell particles are displayed to be stable up to more than 90°C, retaining their original mor-  
333 phology. At a critical temperature, the shell was ruptured, and the core liquid was released. Larger core-shell  
334 particles with thicker shell provide more thermal stability.

### 335 **Declarations**

336 **Funding:** Fariba Malekpour Galogahi acknowledges the support of the higher degree by research (HDR) schol-  
337 arship from Griffith University. Nam-Trung Nguyen acknowledges funding support from the Australian Research  
338 Council through the grant (DP180100055). The devices were fabricated in the Queensland Microtechnology Fa-  
339 cility, part of the Queensland node at Griffith of the Australian National Fabrication Facility, a company estab-  
340 lished under the National Collaborative Research Infrastructure Strategy to provide nano and microfabrication  
341 facilities for Australia's researchers.

342 **Competing interests:** The authors declare that they have no competing interests.

343 **Availability of data and material:** Not applicable

344 **Code availability:** Not applicable

345

### 346 **Reference**

347 Bandara, T., N. T. Nguyen and G. Rosengarten (2015) Slug flow heat transfer without phase change in  
348 microchannels: A review. *Chemical Engineering Science* 283-295. <https://doi.org/10.1016/j.ces.2014.12.007>

349 Carneiro, J., E. Doutel, J. B. L. M. Campos and J. M. Miranda (2016) PDMS droplet formation and  
350 characterization by hydrodynamic flow focusing technique in a PDMS square microchannel. *Journal of*  
351 *Micromechanics and Microengineering* 10:105013. [https://doi.org/Artn\\_105013](https://doi.org/Artn_105013)

352 10.1088/0960-1317/26/10/105013

353 Chong, D. T., X. S. Liu, H. J. Ma, G. Y. Huang, Y. L. Han, X. Y. Cui, J. J. Yan and F. Xu (2015) Advances in  
354 fabricating double-emulsion droplets and their biomedical applications. *Microfluidics and Nanofluidics* 5:1071-  
355 1090. <https://doi.org/10.1007/s10404-015-1635-8>

356 Costa, A. L. R., A. Gomes and R. L. Cunha (2017) Studies of droplets formation regime and actual flow rate of  
357 liquid-liquid flows in flow-focusing microfluidic devices. *Experimental Thermal and Fluid Science* 167-175.  
358 <https://doi.org/10.1016/j.expthermflusci.2017.03.003>

359 Galogahi, F. M., Y. Zhu, H. J. An and N. T. Nguyen (2020) Core-shell microparticles: Generation approaches and  
360 applications. *Journal of Science-Advanced Materials and Devices* 4:417-435.  
361 <https://doi.org/10.1016/j.jsamd.2020.09.001>

362 Good, R. J. and L. Girifalco (1960) A theory for estimation of surface and interfacial energies. III. Estimation of  
363 surface energies of solids from contact angle data. *The Journal of Physical Chemistry* 5:561-565.  
364 <https://doi.org/10.1021/j100834a012>

365 Gorgannezhad, L., K. R. Sreejith, M. Christie, J. Jin, C. H. Ooi, M. Katouli, H. Stratton and N.-T. Nguyen (2020)  
366 Core-Shell Beads as Microreactors for Phylogrouping of *E. coli* Strains. *Micromachines* 8:761.  
367 <https://doi.org/10.3390/mi11080761>

368 Gregory, S. (2018). *Physical properties of glycerine*. *Glycerine*, CRC Press: 113-156.

369 Hu, S. H., D. M. Liu, W. L. Tung, C. F. Liao and S. Y. Chen (2008) Surfactant-Free, Self-Assembled PVA-Iron  
370 Oxide/Silica Core-Shell Nanocarriers for Highly Sensitive, Magnetically Controlled Drug Release and Ultrahigh  
371 Cancer Cell Uptake Efficiency. *Advanced Functional Materials* 19:2946-2955.  
372 <https://doi.org/10.1002/adfm.200800428>

373 Lashkaripour, A., C. Rodriguez, L. Ortiz and D. Densmore (2019) Performance tuning of microfluidic flow-  
374 focusing droplet generators. *Lab on a Chip* 6:1041-1053. <https://doi.org/10.1039/C8LC01253A>

375 Lee, W., L. M. Walker and S. L. Anna (2009) Role of geometry and fluid properties in droplet and thread  
376 formation processes in planar flow focusing. *Physics of Fluids* 3:032103. <https://doi.org/10.1063/1.3081407>

377 Liao, Q. Q., S. K. Zhao, B. Cai, R. X. He, L. Rao, Y. Wu, S. S. Guo, Q. Y. Liu, W. Liu and X. Z. Zhao (2018)  
378 Biocompatible fabrication of cell-laden calcium alginate microbeads using microfluidic double flow-focusing  
379 device. *Sensors and Actuators a-Physical* 313-320. <https://doi.org/10.1016/j.sna.2018.06.006>

380 Lignel, S., A.-V. Salsac, A. Drelich, E. Leclerc and I. Pezron (2017) Water-in-oil droplet formation in a flow-  
381 focusing microsystem using pressure- and flow rate-driven pumps. *Colloids and Surfaces A: Physicochemical and*  
382 *Engineering Aspects* 164-172. <https://doi.org/10.1016/j.colsurfa.2017.07.065>

383 Liu, H. H. and Y. H. Zhang (2009) Droplet formation in a T-shaped microfluidic junction. *Journal of Applied*  
384 *Physics* 3:034906. <https://doi.org/Artn> 034906  
385 10.1063/1.3187831

386 Liu, H. H. and Y. H. Zhang (2011) Droplet formation in microfluidic cross-junctions. *Physics of Fluids* 8:082101.  
387 <https://doi.org/Artn> 082101  
388 10.1063/1.3615643

389 Liu, W., X. L. Yang and W. S. Ho (2011) Preparation of uniform-sized multiple emulsions and micro/nano  
390 particulates for drug delivery by membrane emulsification. *J Pharm Sci* 1:75-93.  
391 <https://doi.org/10.1002/jps.22272>

392 Lu, Y. S., Y. Xia and R. C. Larock (2011) Surfactant-free core-shell hybrid latexes from soybean oil-based  
393 waterborne polyurethanes and poly(styrene-butyl acrylate). *Progress in Organic Coatings* 4:336-342.  
394 <https://doi.org/10.1016/j.porgcoat.2011.03.027>

395 Matsumoto, K., S. Sogabe and T. Endo (2010) Synthesis and Properties of Methacrylate-Based Networked  
396 Polymers Having Ionic Liquid Structures. *Journal of Polymer Science Part a-Polymer Chemistry* 20:4515-4521.  
397 <https://doi.org/10.1002/pola.24242>

398 Mytnyk, S., I. Ziemecka, A. G. L. Olive, J. W. M. van der Meer, K. A. Totlani, S. Oldenhof, M. T. Kreutzer, V.  
399 van Steijn and J. H. van Esch (2017) Microcapsules with a permeable hydrogel shell and an aqueous core  
400 continuously produced in a 3D microdevice by all-aqueous microfluidics. *Rsc Advances* 19:11331-11337.  
401 <https://doi.org/10.1039/c7ra00452d>

402 Nabavi, S. A., G. T. Vladislavljevic and V. Manovic (2017) Mechanisms and control of single-step microfluidic  
403 generation of multi-core double emulsion droplets. *Chemical Engineering Journal* 140-148.  
404 <https://doi.org/10.1016/j.cej.2017.04.008>

405 Nguyen, N. T., S. Schubert, S. Richter and W. Dotzel (1998) Hybrid-assembled micro dosing system using silicon-  
406 based micropump/valve and mass flow sensor. *Sensors and Actuators a-Physical* 1:85-91. <https://doi.org/Doi>  
407 10.1016/S0924-4247(98)00039-9

408 Nie, Z. H., M. S. Seo, S. Q. Xu, P. C. Lewis, M. Mok, E. Kumacheva, G. M. Whitesides, P. Garstecki and H. A.  
409 Stone (2008) Emulsification in a microfluidic flow-focusing device: effect of the viscosities of the liquids.  
410 *Microfluidics and Nanofluidics* 5:585-594. <https://doi.org/10.1007/s10404-008-0271-y>

411 Nisisako, T., S. Okushima and T. Torii (2005) Controlled formulation of monodisperse double emulsions in a  
412 multiple-phase microfluidic system. *Soft Matter* 1:23-27. <https://doi.org/10.1039/b501972a>

413 Rahimi, M., A. S. Khorrami and P. Rezai (2019) Effect of device geometry on droplet size in co-axial flow-  
414 focusing microfluidic droplet generation devices. *Colloids and Surfaces A: Physicochemical and Engineering*  
415 *Aspects* 510-517. <https://doi.org/10.1016/j.colsurfa.2019.03.067>

416 Rausch, M. H., L. Kretschmer, S. Will, A. Leipertz and A. P. Froba (2015) Density, Surface Tension, and  
417 Kinematic Viscosity of Hydrofluoroethers HFE-7000, HFE-7100, HFE-7200, HFE-7300, and HFE-7500. *Journal of*  
418 *Chemical and Engineering Data* 12:3759-3765. <https://doi.org/10.1021/acs.jced.5b00691>

419 Sreejith, K. R., L. Gorgannezhad, J. Jin, C. H. Ooi, T. Takei, G. Hayase, H. Stratton, K. Lamb, M. Shiddiky, D.  
420 V. Dao and N. T. Nguyen (2020) Core-Shell Beads Made by Composite Liquid Marble Technology as A Versatile  
421 Microreactor for Polymerase Chain Reaction. *Micromachines (Basel)* 3:242. <https://doi.org/10.3390/mi11030242>

422 Takei, T., Y. Yamasaki, Y. Yuji, S. Sakoguchi, Y. Ohzuno, G. Hayase and M. Yoshida (2019) Millimeter-sized  
423 capsules prepared using liquid marbles: Encapsulation of ingredients with high efficiency and preparation of  
424 spherical core-shell capsules with highly uniform shell thickness using centrifugal force. *Journal of Colloid and*  
425 *Interface Science* 414-423. <https://doi.org/10.1016/j.jcis.2018.10.058>

426 Tan, J., J. H. Xu, S. W. Li and G. S. Luo (2008) Drop dispenser in a cross-junction microfluidic device: Scaling  
427 and mechanism of break-up. *Chemical Engineering Journal* 2-3:306-311.  
428 <https://doi.org/10.1016/j.cej.2007.04.011>

429 Teo, A. J. T., F. Malekpour-Galogahi, K. R. Sreejith, T. Takei and N. T. Nguyen (2020) Surfactant-free, UV-  
430 curable core-shell microcapsules in a hydrophilic PDMS microfluidic device. *Aip Advances* 6:065101.  
431 <https://doi.org/10.1063/5.0004736>

432 Utada, A. S., E. Lorenceau, D. R. Link, P. D. Kaplan, H. A. Stone and D. A. Weitz (2005) Monodisperse double  
433 emulsions generated from a microcapillary device. *Science* 5721:537-541.  
434 <https://doi.org/10.1126/science.1109164>

435 Wang, H., H. Liu, H. Liu, W. Su, W. Chen and J. Qin (2019) One-Step Generation of Core-Shell Gelatin  
436 Methacrylate (GelMA) Microgels Using a Droplet Microfluidic System. *Advanced Materials Technologies*  
437 6:1800632. <https://doi.org/10.1002/admt.201800632>

438 Ward, T., M. Faivre, M. Abkarian and H. A. Stone (2005) Microfluidic flow focusing: drop size and scaling in  
439 pressure versus flow-rate-driven pumping. *Electrophoresis* 19:3716-3724.  
440 <https://doi.org/10.1002/elps.200500173>

441 Wei, Y., S. Soh, M. M. Apodaca, J. Kim and B. A. Grzybowski (2010) Sequential reactions directed by core/shell  
442 catalytic reactors. *Small* 7:857-863. <https://doi.org/10.1002/sml.200902336>

443 Xie, M.-Y., L. Yu, H. He and X.-F. Yu (2009) Synthesis of highly fluorescent LaF<sub>3</sub>: Ln<sup>3+</sup>/LaF<sub>3</sub> core/shell  
444 nanocrystals by a surfactant-free aqueous solution route. *Journal of Solid State Chemistry* 3:597-601.  
445 <https://doi.org/10.1016/j.jssc.2008.12.011>

446 Xiong, H. M., X. Y. Guan, L. H. Jin, W. W. Shen, H. J. Lu and Y. Y. Xia (2008) Surfactant-free synthesis of  
447 SnO<sub>2</sub>@PMMA and TiO<sub>2</sub>@PMMA core-shell nanobeads designed for peptide/protein enrichment and MALDI-  
448 TOF MS analysis. *Angewandte Chemie-International Edition* 22:4204-4207. <https://doi.org/DOI>  
449 10.1002/anie.200705942

450 Xu, S. and T. Nisisako (2020) Polymer Capsules with Tunable Shell Thickness Synthesized via Janus-to-core  
451 shell Transition of Biphasic Droplets Produced in a Microfluidic Flow-Focusing Device. *Sci Rep* 1:4549.  
452 <https://doi.org/10.1038/s41598-020-61641-8>

453 Yap, Y. F., S. H. Tan, N. T. Nguyen, S. M. S. Murshed, T. N. Wong and L. Yobas (2009) Thermally mediated  
454 control of liquid microdroplets at a bifurcation. *Journal of Physics D-Applied Physics* 6:065503.  
455 <https://doi.org/Artn> 065503

456 10.1088/0022-3727/42/6/065503

457 Zheng, J., C. Cheng, W.-J. Fang, C. Chen, R.-W. Yan, H.-X. Huai and C.-C. Wang (2014) Surfactant-free  
458 synthesis of a Fe<sub>3</sub>O<sub>4</sub>@ZIF-8 core-shell heterostructure for adsorption of methylene blue. *CrystEngComm*  
459 19:3960-3964. <https://doi.org/10.1039/C3CE42648C>

460